RESEARCH ARTICLE

Key Points:
- Ensemble regional projections show a significant increase in frequency and intensity of heat stress indices, heat waves, and tropical nights
- Changes in temperature, humidity, and heat stress indices are characterized by robust patterns in terms of diurnal and regional variations

Correspondence to:
J.-B. Ahn,
jbahn@pusan.ac.kr

Worsening of Heat Stress Due To Global Warming in South Korea Based on Multi-RCM Ensemble Projections

Eun-Soon Im[1] [iD], **Yeon-Woo Choi[2]** [iD], and **Joong-Bae Ahn[2]** [iD]

[1]Department of Civil and Environmental Engineering/Division of Environment and Sustainability, Hong Kong University of Science and Technology, Hong Kong, [2]Division of Earth Environmental System, Pusan National University, Busan, South Korea

Abstract This study assesses the future changes in summer (June–July–August; JJA) heat stress over South Korea under global warming. To better resolve the region-specific changes in terms of geographical patterns and severity of heat stress in the Korean peninsula, four regional climate models (RCMs) are used for dynamical downscaling of Hadley Centre Global Environmental Model version 2—Atmosphere and Ocean global projections forced by two Representative Concentration Pathway (RCP4.5 and RCP8.5) scenarios. Dynamically downscaled simulations (horizontal resolution of 12.5 km and output interval of 3 h) facilitate in-depth analysis of diurnal variation and extremes over South Korea, as well as focusing on the particular location, Daegu, that is characterized by high vulnerability to rising temperature. Both maximum temperature and heat stress indices such as wet bulb globe temperature and apparent temperature, which include the effect of humidity, are examined in order to comprehensively interpret the behaviors of heat stress in response to anthropogenic climate change. Ensemble projections reveal robust patterns of temperature and resultant humidity increases that are roughly constrained by the approximate 7%/K increase in the moisture holding capacity. The changes in temperature and humidity are directly transmitted to the heat stress indices, showing a significant increase. The heat stress is exacerbated in a differentiated way, with more intensification in diurnal variation at nighttime and in regional variation at low-elevation basins. Both RCP4.5 and RCP8.5 scenarios project the statistical likelihood of a notable increase of extreme heat stress indices, much stronger and more extended heat waves, and the emergence of a long period of consecutive tropical nights.

1. Introduction

Intense and frequent heat waves accompanied by global warming can worsen the risk of human health and heat-related mortality. As the global average temperature for 2016 was the highest on record and marks consecutive record-breaking values (Climate Council, 2016), global concerns that the climate system is warming up faster than expected may be well founded (IPCC, 2013). In accordance with global warming, Korea also experienced one of its hottest summers in 2016 (Korea Meteorological Administration (KMA), 2017). The number of heat waves, which are defined as consecutive days with maximum temperature exceeding 33°C by the Korea Meteorological Administration (KMA), in 2016 was the second highest ever recorded in the observational data, following the worst one with a death toll exceeding 3,300 that occurred in the summer of 1994 (Kysely & Kim, 2009).

A significant body of research has investigated the impacts of anthropogenic climate change on extreme heat events with a focus on temperature (e.g., Meehl & Tebaldi, 2004). However, the high risk arising from heat stress is not a function of the intensity of temperature alone, but the combined consequences of temperature and humidity (Davis et al., 2016; Fischer et al., 2012; Im et al., 2017; Sherwood & Huber, 2010; Willett & Sherwood, 2012). Since high humidity tends to reduce the efficiency of the human body's cooling system by inhibiting sweat evaporation, the humidity level can play a critical role in making extreme heat much more dangerous and intolerable (Sherwood & Huber, 2010; Willett & Sherwood, 2012). Furthermore, Wu et al. (2017) emphasized the effect of wind speed to measure the human thermal perception, showing that decreases in wind speed worsen the heat stress during the summer in the warm region of China.

The climate of South Korea in the summer season is particularly vulnerable to the negative impact of global warming in terms of heat stress because the typical summer weather condition is characterized by heat and humidity under the influence of predominant southwesterly monsoon flows (Suh & Kim, 2015). As global

warming is attributable to overall moistening (Willett et al., 2008), the projected temperature increase will exacerbate the severity of heat stress very close to the dangerous level of human adaptability. Nevertheless, relatively few studies have explicitly addressed the contribution of humidity to extreme heat stress due to anthropogenic climate change focusing on the Korean peninsula, whereas most previous studies have analyzed the likelihood of extremes based on maximum temperature (e.g., Boo et al., 2006; Im et al., 2015, 2011; Koo et al., 2009; Min et al., 2014). Recently, several studies using Global Climate Models (GCMs) have dealt with the issue of heat stress using various indices that measure the combined effects of temperature and humidity (e.g., Buzan et al., 2015; Fischer & Knutti, 2013; Sherwood & Huber, 2010; Willett & Sherwood, 2012; Zhao et al., 2015), but it is difficult for GCMs with 100–200 km resolution to account for the unique geographical properties that potentially modulate the regional variation and intensity of heat stress in South Korea.

In this study, we investigate the changes in extreme heat stress in response to anthropogenic warming using multiregional climate model (RCM) ensemble projections. In order to produce fine-scale (12.5 km) regional projections suitable for resolving complex topography and coastlines, which are poorly represented in a coarse grid GCM, dynamical downscaling is performed using four different RCMs, namely, WRF, HadGEM3-RA, RegCM4, and MM5, driven by the Hadley Centre Global Environmental Model version 2—Atmosphere and Ocean (HadGEM2-AO) global projections under the two representative concentration pathway (RCP4.5 and RCP8.5) scenarios (see section 2.1). Temperature and humidity from twelve 30 year reference (1981–2010) and RCP4.5 and RCP8.5 future (2071–2100) projections are analyzed based on the output of 3 h interval and 12.5 km spatial resolutions. Although systematic biases appear in the downscaled simulations (see section 3.1), bias correction was not applied in this study. The systematic bias of each model can be partly eliminated by subtracting the climatological mean of the reference simulation from that of the RCP future projection, under the assumption of "stationarity," that is, the bias pattern does not change with time. Suh et al. (2016) demonstrated using the same RCM projections used in this study that changes in temperature do not vary greatly between without and with bias-corrected projections, in contrast with the significant difference in the performance of the reference simulation. However, the extreme analysis counting of exceedance based on absolute threshold may be affected by the cold bias. In this regard, the number of days with tropical nights (minimum temperature over 25°C) and hot days (maximum temperature over 33°C) may be underestimated due to systematic cold bias. In spite of this caveat, comparing three simulations (i.e., Reference, and RCP4.5 and RCP8.5 scenarios) gives us some insight into the changes in heat stress in response to different levels of greenhouse gas (GHG) emissions. As for an effective indicator to measure extreme heat stress, we calculate and characterize the simplified wet bulb globe temperature (Willett & Sherwood, 2012) and apparent temperature (Steadman, 1984), which are popular heat stress indices that include the effect of humidity (see section 2.2). In addition to heat stress indices, the duration of heat waves (defined as consecutive days with maximum temperature exceeding 33°C) and tropical nights (defined as minimum temperature exceeding 25°C) are examined in order to comprehensively interpret future changes in extreme heat stress.

2. Experimental Design and Analysis Method

2.1. RCM Experimental Design

In this study, four RCMs (WRF, RegCM4, MM5, and HadGEM3-RA) are used for regional climate simulations over Northern East Asia within the framework of a national downscaling project of the Republic of Korea. All RCMs are performed under the same horizontal grid resolution (12.5 km) and domain configuration. Figure 1 presents the domain and topography that are commonly configured for four-RCM simulations. The domain covers Northern East Asia centered at the Korean peninsula (center: 37.5°N, 127.5°E), and the 12.5 km grid spacing is fine enough to represent the general geographical settings, such as relevant mountains located in South Korea (e.g., the Taebaek Mountains, extending from north to south along the eastern coastal regions of Korea, and the Sobaek Mountains located in the south-central regions of the peninsula). On the other hand, the topography of HadGEM2-AO (1.875° × 1.250°) over the RCM domain shows hardly any mountain slope in the Korean peninsula. This poor representation of geographical characteristics could negatively affect the model performance in simulating local and regional climates. All RCMs are driven by the same initial and lateral boundary conditions derived from the Hadley Centre Global Environmental Model version 2—Atmosphere and Ocean (HadGEM2-AO) model data (Baek et al., 2013). Previous studies
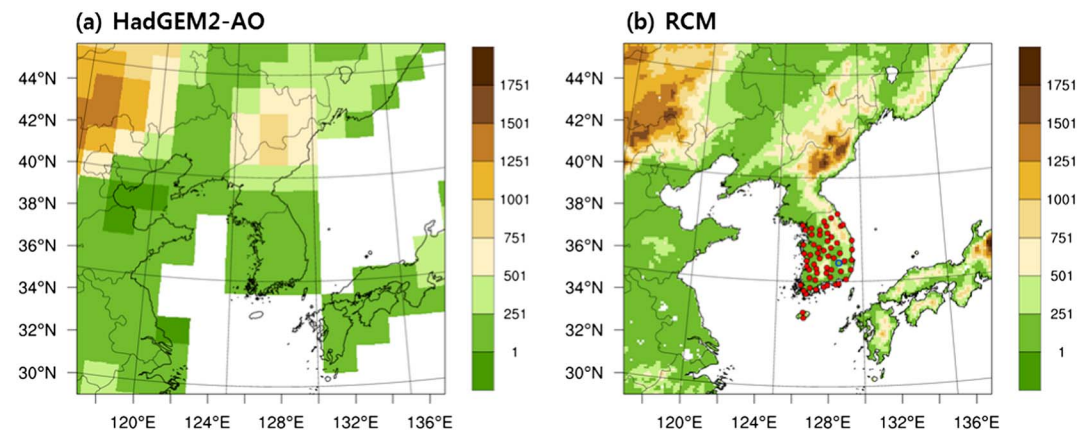
Figure 1. Topography (unit: m) used for HadGEM2-AO (1.875° × 1.25°) and RCM simulations over the RCM domain. The 59 weather stations (58 red closed circles and 1 blue open circle) are used to validate the reference simulations. Daegu station denoted by the blue open circle is specifically used to validate the extremes of heat waves and heat stress indices.

have shown that HadGEM2-AO exhibits better performance in simulating climate over Northeast Asia, compared to other CMIP models (CMIP3 and CMIP5) (Baek et al., 2013; Hong & Ahn, 2015). The four individual RCMs use different physical parameterization components, which result in the intermodel spread (i.e., uncertainty) among the models. This model uncertainty is well discussed by Hawkins and Sutton (2009). They suggested that uncertainties in projections of future climate arise from various sources, mostly referred to future emissions of GHG (scenario uncertainty), choice of climate model (model uncertainty), and internal variability. An important point is that the relative contributions of uncertainty sources were found to vary considerably depending on the lead time. For example, the projection with more than 60 year lead time like our study shows larger factions of model uncertainty than internal variability.

A more detailed description of the RCMs is presented in Table 1. The two RCP scenarios, namely, RCP4.5 and RCP8.5 (Moss et al., 2010), are used for future projection. The reference simulations have been integrated over the period 1979–2010, and RCP4.5 and RCP8.5 projections have been integrated from 2019 to 2100. Since the CMIP5 historical simulations ended in 2005, the reference simulations for the period 2006–2010 are forced by RCP8.5 emission scenario. GHG concentrations for this 5 year period do not vary greatly depending on the scenarios, such as 384.82 ppm for RCP4.5 and 384.87 ppm for RCP8.5. A 2 year spin-up period for the reference and RCP simulations (1979–1980 and 2019–2020, respectively) is excluded from the analysis for the typical summer season (June–July–August; JJA). Two sets of 30 year simulations have been analyzed: one for the present period of 1981–2010 and one for the future of 2071–2100.

To validate the reference simulations, 3 h meteorological data from 59 weather stations (58 red closed circles and 1 blue open circle in Figure 1) operated by the KMA are used for the same period of reference simulations. These station data make it possible to validate diurnal variation and to perform the in-depth analysis

Table 1

List of the Four Regional Climate Models (RCMs) Used in This Study and Their Configurations

	WRF	RegCM4	MM5	HadGEM3-RA
Institute	Pusan National University	Kongju National University	Ulsan National Institute of Science and Technology	National Institute of Meteorological Sciences
Dynamic framework	Nonhydrostatic	Hydrostatic	Nonhydrostatic	Nonhydrostatic
Vertical coordinate/levels	Eta/28	Sigma/23	Sigma/24	Hybrid/38
Convection scheme	Kain-Fritsch II	MIT-Emanuel	Kain-Fritsch II	Revised mass flux scheme
Land surface	Noah	CLM3.5	CLM3.0	MOSES-I
LWR scheme	CAM	CCM3	CCM2	Generalized 2-stream
SWR scheme	CAM	CCM3	CCM2	Generalized 2-stream
Spectral nudging	No	Yes	Yes	No
References	Skamarock et al. (2008)	Giorgi et al. (2012)	Cha and Lee (2009)	Davies et al. (2005)

of each particular location. The model output of 3 h interval with 12.5 km horizontal resolution is interpolated into 59 observational sites using an inverse distance weight interpolation method. In addition, a daily mean gridded temperature data set with 0.5° × 0.5° grid generated by Asian Precipitation-Highly-Resolved Observational Data Integration Toward Evaluation (APHRODITE) project (Yasutomi et al., 2011) is also used for the validation of reference simulations. For this validation, the model output is also interpolated into the same grid with APHRODITE using an inverse distance weight interpolation method.

2.2. Analysis Method

Various heat stress indices have been developed, each suited for a specific purpose (Anderson et al., 2013; Buzan et al., 2015). They are mostly calculated based on the combination of meteorological variables such as temperature, humidity, radiation, and wind. In general, the algorithms for combining multiple variables are approximately derived with many assumptions. In addition, since most heat stress indices include many constants derived from an empirical fit for a particular circumstance (e.g., the target region's climatological condition), finding a single index that is universally applicable is problematic (Willett & Sherwood, 2012). In this study, we select two popular heat stress indices, namely, simplified wet bulb globe temperature and apparent temperature, in order to measure the physiological thermal comfort.

Original wet bulb globe temperature is an index composed of air temperature, natural wet bulb temperature, and black globe temperature. It has the advantage of providing the threshold to levels of physical activities (Dunne et al., 2013; Willett & Sherwood, 2012) and is considered a well-established heat index for workplace applications (Lemke & Kjellstrom, 2012). However, it is difficult to calculate the wet bulb globe temperature using conventional climate model output. For convenience and easy application, we select simplified wet bulb globe temperature (T_{sw}), which is an approximation to the wet bulb globe temperature that assumes moderately high radiation levels and light wind conditions. Simply, T_{sw} can be calculated using only temperature and humidity without accounting for the effect of radiative fluxes and wind (Willett & Sherwood, 2012). The formula to calculate T_{sw} is as follows.

$$T_{sw} = 0.567 T_{as} + 0.393 e + 3.94,$$

where T_{as} is air temperature (°C) and e is vapor pressure (hPa).

To examine the robustness of the characteristics of heat stress, we also calculate the apparent temperature (hereafter, T_{ap}), which is widely used as an indicator of heat comfort. T_{ap} is a measure of perceived temperature, incorporating human physiology and the body's ability to dissipate heat, and is therefore considered a physiologically based heat stress index suitable for quantifying sultriness during a heat wave (Steinweg & Gutowski, 2015). There are several ways to estimate T_{ap} (Davis et al., 2016), but we follow the method adopted by Steinweg and Gutowski (2015).

$$T_{ap} = 2.719 + 0.944(T_{as}) + 0.016(T_d)^2,$$

where T_{as} is air temperature (°C) and T_d is dewpoint temperature (°C).

In addition to these two different heat stress indices that include the effect of humidity, we investigate the characteristics of heat waves and tropical nights, which are defined by only maximum and minimum temperature, respectively. Whereas T_{sw} and T_{ap} are not specifically developed and adjusted for South Korea's climate condition, the thresholds to define heat waves (maximum T_{as} exceeding 33°C) and tropical nights (minimum T_{as} exceeding 25°C) are determined based on the current standards applied by KMA. The KMA has issued heatwave warnings in the case of two consecutive days with maximum temperature exceeding 33°C.

3. Results

3.1. Validation of Reference Simulation

Since the previous studies evaluated the general skills of the four individual RCMs used in this study (e.g., Hong & Ahn, 2015; Im et al., 2015; Lee et al., 2014; Seo et al., 2015; Suh et al., 2016), we only compare the performance of four-RCM ensemble mean (hereafter, ENS) in capturing the summer season (June–July–August: JJA) climatology of T_{as}, T_{sw}, and T_{ap}, which are focused on this study, with driving GCM as well as observations.
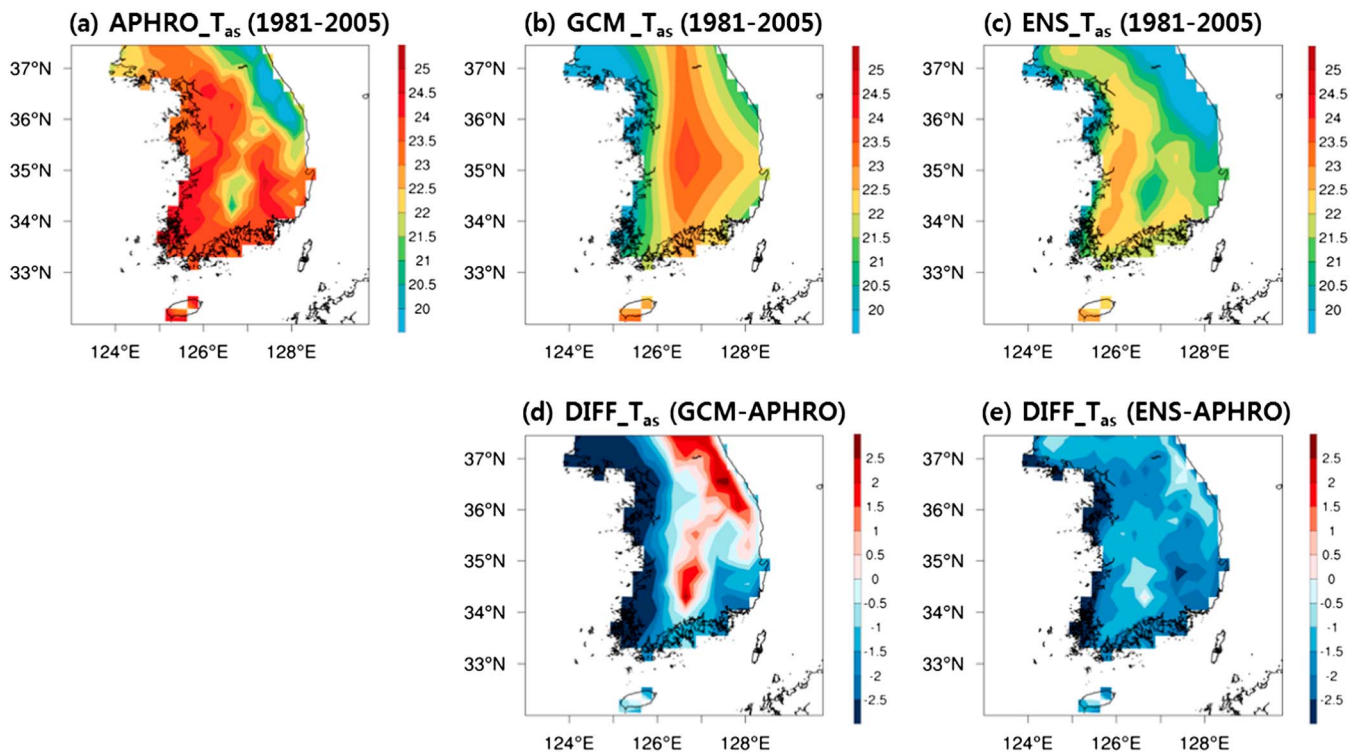
Figure 2. Spatial distribution of (a, b, c; unit: °C) climatological mean temperature derived from APHRODITE observation, HadGEM2-AO, and ENS reference simulations, (d, e) and their differences in the summer season (JJA).

First, we present the spatial distribution of 25 year (1981–2005) JJA climatological mean T_{as} derived from APHRODITE observation, HadGEM2-AO, and ENS (Figure 2). To facilitate the comparison, HadGEM2-AO and ENS with different resolutions are interpolated onto a 0.5° × 0.5° APHRODITE grid using a bilinear interpolation method. The relevant feature derived from this comparison is that the spatial pattern of temperature simulated by HadGEM2-AO is completely distorted against APHRODITE observation. The difference pattern between GCM and APHRODITE clearly reflects the main cause of this distortion, indicating systematic positive bias along the mountainous regions but systematic negative bias along the low-lying coastal regions. On the other hand, ENS is capable of reproducing topographically induced spatial distribution of the temperature that is similar with the observed pattern. Since temperature exhibits a strong gradient with altitude following the lapse rate, the fine scale of ENS can better resolve the distinct topographical signature and thus enhance the performance in capturing the temperature distribution. However, ENS systematically underestimates T_{as} across the whole domain, mostly within the range of −1°C and −2°C.

Next, we present the spatial distribution of 30 year (1981–2010) JJA climatological daily mean T_{as}, T_{sw}, and T_{ap} derived from the station observations and ENS at 59 in situ observational sites (Figure 3). To facilitate the comparison, ENS with 12.5 km resolution is again interpolated into 59 observational sites using an inverse distance weight interpolation method. Topographical effect seen clearly in Figure 2 seems to be less relevant in the observed pattern at the individual station base. It is due to the relatively low density of high-elevation stations. Although T_{as}, T_{sw}, and T_{ap} simulated by ENS agree reasonably well with those from the observations, they reveal the systematic underestimation across the whole domain. Since the negative bias of simulated T_{as} is transmitted to T_{sw} and T_{ap}, they retain a similar pattern of negative bias. However, the magnitude of the negative bias tends to be moderated or amplified according to the relative contribution of humidity because T_{sw} and T_{ap} are defined as a function of not only temperature but also humidity.

Furthermore, in order to quantitatively evaluate the performance of reference simulations, we applied the Taylor diagrams (Figure 4). By comparing RCM simulations with in situ observational data, the HadGEM3-RA commonly shows the largest standard deviation in T_{as}, T_{sw}, and T_{ap} among the four RCMs, while standard deviations derived from the WRF model agree relatively well with those of the station observation. As for the
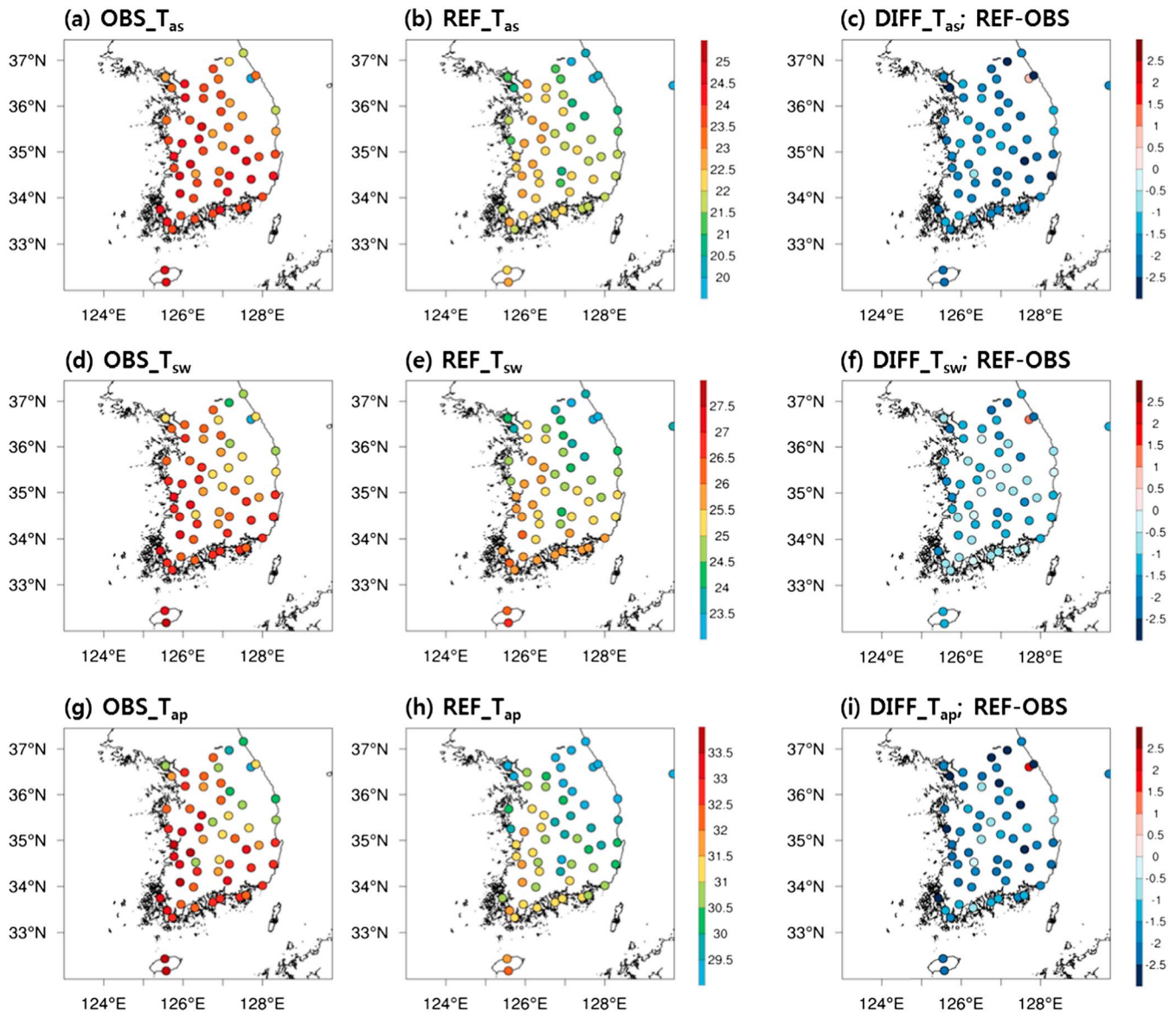
Figure 3. Spatial distribution of (a, b; unit: °C) climatological daily mean temperature, (d, e, unit: °C) simplified wet bulb globe temperature, and (g, h, unit: °C) apparent temperature derived from 59 observational stations and ENS reference simulations in the summer season (JJA). The model output is interpolated into 59 observational station sites, (c, f, and i) and differences between ENS simulation and observation are then calculated.

spatial correlation, ENS generally outperforms the four individual RCMs regardless of variables such as T_{as}, T_{sw}, and T_{ap}. In order to support these results based on the in situ observational data, we also used the daily temperature data from the APHRODITE for the overlapping periods from 1981 to 2005. By comparing RCM simulations with APHRODITE data set, ENS shows a relatively better performance in simulating the spatial distribution of T_{as}, T_{sw}, and T_{ap} in terms of spatial correlation, compared to the results from the four individual RCMs, which is in line with the above results based on the in situ observational data.

Figure 5 presents the diurnal variation of T_{as}, T_{sw}, and T_{ap} averaged over 59 locations derived from the observations and RCM simulations. As for the model simulations, since ENS mean may smooth the data variability, we present together the ENS (thick blue line) and the four RCM spreads between the maximum and minimum values of each RCM (sky-blue shading) in order to provide the uncertainty range introduced by each RCM (i.e., intermodel spread). T_{as}, T_{sw}, and T_{ap} exhibit relevant diurnal variation with a daily minimum at 0600 local time (LT) and daily maximum at 1500 LT. By comparing with the observed pattern, ENS simulates
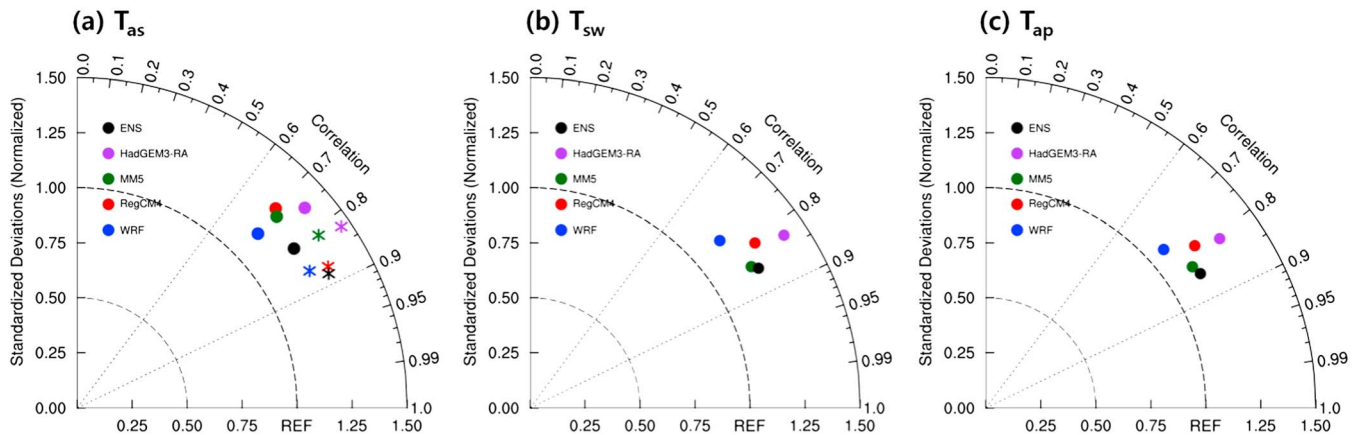
Figure 4. Comparison of JJA mean (a, unit: °C) T_{as}, (b, unit: °C) T_{sw}, and (c, unit: °C) T_{ap} between the four individual RCM simulations and their ENS mean and observations through Taylor diagram. The closed circle (asterisk) indicates the comparison between RCM simulations and 59 in situ observational data (APHRODITE data set). Radial axes show temporal standard deviation, normalized against that of the observations, and the arc denotes the spatial correlation coefficient.

the phase of the diurnal cycle reasonably well, capturing both maximum and minimum peaks. However, consistent with the cold bias presented in the daily mean spatial pattern, ENS manifests a cold bias in the diurnal variation of T_{as}, T_{sw}, and T_{ap}. Interestingly, ENS shows better performance in daytime than in nighttime. This cold bias of the daily mean mostly occurs during the nighttime. During the daytime, ENS becomes closer to the observational data, indicating that the bias of the maximum value is relatively less.

On the gross pattern of diurnal cycles of T_{as}, T_{sw}, and T_{ap}, we then focus on the detailed characteristics of maximum T_{as}, T_{sw}, and T_{ap} because of their relevant association with extreme heat stress. Figure 6 presents the probability density function of daily maximum T_{as}, T_{sw}, and T_{ap} derived from the observations and simulation. T_{as}, T_{sw}, and T_{ap} show different statistical characteristics in terms of mean and variance. For example, the means (variance) of T_{as}, T_{sw}, and T_{ap} derived from simulation are 26°C, 28°C, and 35°C (8.4, 9.4, and 18.7), respectively, which are in good agreement with observation. In spite of the slight shift in distributions toward the left side due to the cold bias, the simulations are capable of capturing the different behavior corresponding to observed T_{as}, T_{sw}, and T_{ap}, not only for the relative probability varying at particular range of values but also the variation range. Particularly, T_{as}, T_{sw}, and T_{ap} derived from observations and simulation are fairly normally distributed but with a slightly negative skewness and a very mild negative kurtosis. The quantitative assessments of the statistics are summarized in Table 2. Consistent with the diurnal variation of temperature seen in Figure 5, T_{sw} shows better performance than T_{as} and T_{ap}, in terms of negative bias.
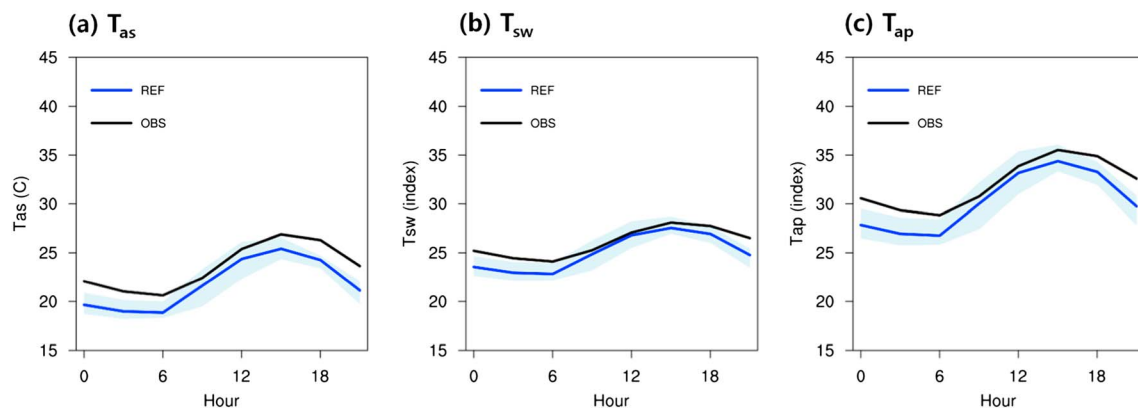

Figure 5. Diurnal variations in summer mean (a, unit: °C) T_{as}, (b, unit: °C) T_{sw}, and (c, unit: °C) T_{ap} averaged over 59 stations derived from observations and ENS reference simulations. The blue line indicates ENS of the four RCMs, and the sky-blue shading shows the intermodel spread between the maximum and minimum values among the four RCMs.
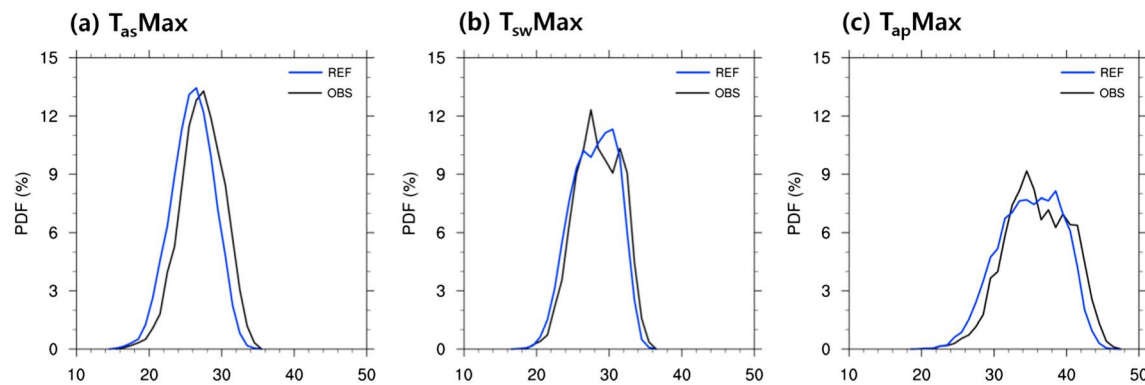
Figure 6. Probability density function of daily maximum (a, unit: °C) T_{as}, (b, unit: °C) T_{sw}, and (c, unit: °C) T_{ap} averaged over 59 stations derived from observations and reference simulations in the summer season.

To further assess how well the models are able to simulate the extreme heat waves occurring in the present-day climate, we compare the simulated frequency and intensity of heat waves with the observed pattern. For this analysis, we select one particular station, namely, Daegu (latitude: 35.89°N, longitude: 128.62°E, altitude: 49 m), rather than averaged or pooled over 59 stations. Since the severity of heat waves and their impact on mortality show a strong regional dependency (Kim et al., 2006), the analysis from all 59 stations might lead to imperceived interpretation of the high levels of heat stress that already exist in some parts of South Korea. Daegu, one of the hottest cities in Korea, is located in a basin surrounded by mountains (see Figure 1), and this geographical setting may contribute to its higher temperature than the surrounding higher elevation areas. Figure 7 shows the frequency of consecutive hot days in Daegu derived from the observations and simulations. As mentioned in section 2.2, a hot day is defined as a day with maximum T_{as} exceeding 33°C, which is the threshold applied by KMA for issuing heat wave warnings. Figure 7 also includes the intensities of heat waves that are calculated as maximum T_{as} averaged over the spells of each duration class. ENS is capable of reproducing the qualitative characteristics of heat waves, corresponding to frequency and intensity. Similar to the observed pattern, the frequency of heat waves gradually decreases but their intensity increases as the interval length increases. However, ENS consistently underestimates the frequency of heat waves, in spite of the existence of a model result with higher frequency than the observed values (upper end of the spread bar). This is because the absolute threshold (i.e., 33°C) does not allow consideration for the degree of the bias. Therefore, individual model results can be rather sensitive to the predefined threshold according to their bias in the model climatology.

Moving to the extremes of heat stress indices, we examine the RCM performance to simulate the threshold exceedance of T_{sw} and T_{ap} for present-day climate. Whereas the threshold of 32°C is applied to maximum T_{sw} in order to describe the level of extreme risk (Willett & Sherwood, 2012), the threshold of 40.6°C is used to count maximum T_{ap} based on the criterion used by the U.S. National Weather Service in issuing a heat advisory warning because of dangerous health conditions (Fischer & Schar, 2010; Steinweg & Gutowski, 2015). Figure 8 presents the total number of threshold exceedances of maximum T_{sw} and maximum T_{ap} in Daegu for the 30 year summer season (JJA) derived from the observations and reference simulation. Analysis of the observational data shows that Daegu has experienced 648 days with maximum T_{sw} exceeding the threshold of 32°C during the recent 30 year summer season (JJA) in the total of 2760 days (92 d/yr × 30 years). This average of 21.6 days annually demonstrates that Daegu is already exposed to a vulnerable condition in terms of human thermal comfort and heat-related mortality. This suggests that a few degrees of future warming will worsen the heat stress adaptability. Compared to the threshold exceedance counted by the observational data, ENS shows fewer extremes in both T_{sw} and T_{ap}. However, the intermodel spread shows an RCM with more threshold exceedances than the observations. Similar to the analysis of heat waves, the absolute threshold causes a large deviation in the individual models, depending on the systematic bias in their climatology. Considering that this comparison

Table 2
The Statistics of Daily Maximum T_{as} (unit: °C), T_{sw} (unit: °C), and T_{ap} (unit: °C) Averaged Over 59 Stations Derived From Observations (Parentheses) and Reference Simulations (Nonparentheses) in JJA season

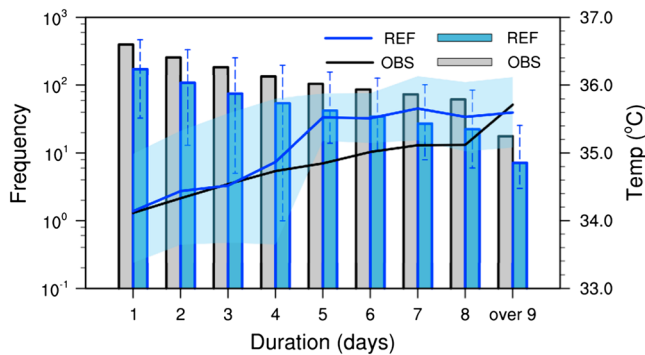|	Mean	Variance	Skewness	Kurtosis
T_{as}	26.0 (27.2)	8.4 (8.6)	−0.2 (−0.2)	−0.2 (−0.1)
T_{sw}	28.0 (28.5)	9.4 (9.4)	−0.2 (−0.1)	−0.7 (−0.6)
T_{ap}	35.0 (36.0)	18.7 (19.0)	−0.2 (−0.1)	−0.6 (−0.5)

Figure 7. Frequency distribution of consecutive hot days in Daegu station (blue open circle in Figure 1) in the summer season as a function of duration. The lines indicate the daily maximum T_{as} (unit: °C) averaged over the spells of each duration class derived from observations and ENS simulation. The four RCM spreads for frequency (bar) and intensity (line) are described by error bar and shading, respectively.

is based on pointwise and extreme climate analysis, we considered ENS to have shown encouraging performance in simulating the detailed characteristics of heat stress in Daegu, which is one of the hottest cities in Korea.

The validation of the reference simulation against station observations demonstrates that ENS from the four RCMs shows reasonable performance in reproducing both the observed climatological statistics across various temporal and spatial scales and the distinct characteristics among T_{as}, T_{sw}, and T_{ap}. However, ENS manifests a systematic cold bias in T_{as} pattern, and this error is transmitted to T_{sw} and T_{ap}. Since severe cold bias along the mountainous regions is partly due to the sparse density of observational station data, the analysis focusing solely on the Daegu station located in a low basin area shows a reasonable performance in capturing the extremes of heat waves and heat stress indices. Given that vulnerability to heat stress is dominant in highly populated urban cities and particularly low-altitude basins (Kim et al., 2006; Son et al., 2012), this result supports the potential usefulness of ENS projections for preparing for and minimizing the adverse human health and mortality consequences.

3.2. Projection of Future Changes

In this section, we focus on the future projection of heat stress in response to different emission scenarios. Figures 9 and 10 present the spatial distribution of the future changes in T_{as}, T_{sw}, T_{ap}, and specific humidity derived from ENS and HadGEM2-AO projections under the RCP4.5 and RCP8.5 scenarios at the end of the 21st century (2071–2100) with respect to the present-day climate (1981–2010). The warming projected by ENS is slightly lower than that from HadGEM2-AO. For example, ENS and HadGEM2-AO under RCP4.5 (RCP8.5) scenarios project temperature increases of 2.8°C (4.5°C) and 3.2°C (5.1°C), respectively. Accordingly, HadGEM2-AO shows a slightly larger increase in heat indices than ENS does. However, the difference between HadGEM2-AO and ENS seems to be marginal compared to the increases in temperature and heat indices in response to enhanced GHGs concentrations. In line with many other studies (e.g., Suh et al., 2016; Ahn, Hong, et al., 2016; Ahn, Jo, et al., 2016), temperature increases are very clear and unequivocal across the entire target region, and these changes all satisfy the statistical significance at the 95% confidence interval based on the two-tailed t test. The common feature appearing in all T_{as}, T_{sw}, and T_{ap} data is an increasing rate that is roughly proportional to the GHG concentrations. Without exception, T_{as}, T_{sw}, and T_{ap} are all much warmer under RCP8.5 scenario than under RCP4.5 scenario. These temperature changes seem to be monotonically responding to emission forcing. However, a detailed examination of the spatial pattern reveals the important
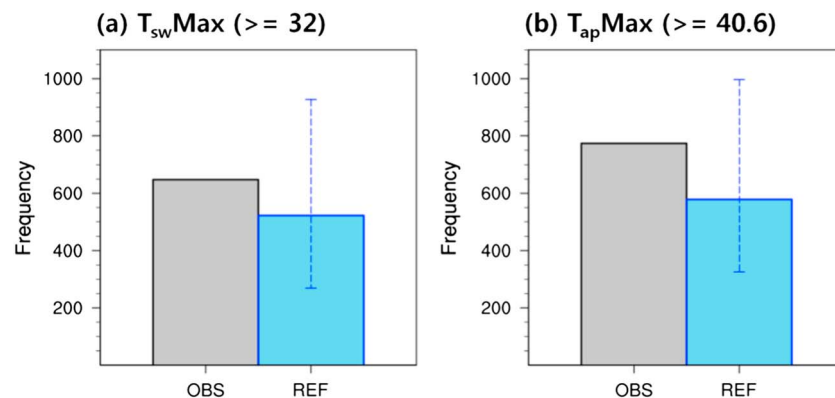

Figure 8. Total number of maximum T_{sw} (unit: °C) exceeding the threshold of 32°C and maximum T_{ap} (unit: °C) exceeding the threshold of 40.6°C in the 30 year (1981–2010) summer season in Daegu station. The blue bar denotes the ENS and the vertical error bar in the middle of the blue box indicates the intermodel spread between the maximum and minimum values among the four RCMs.
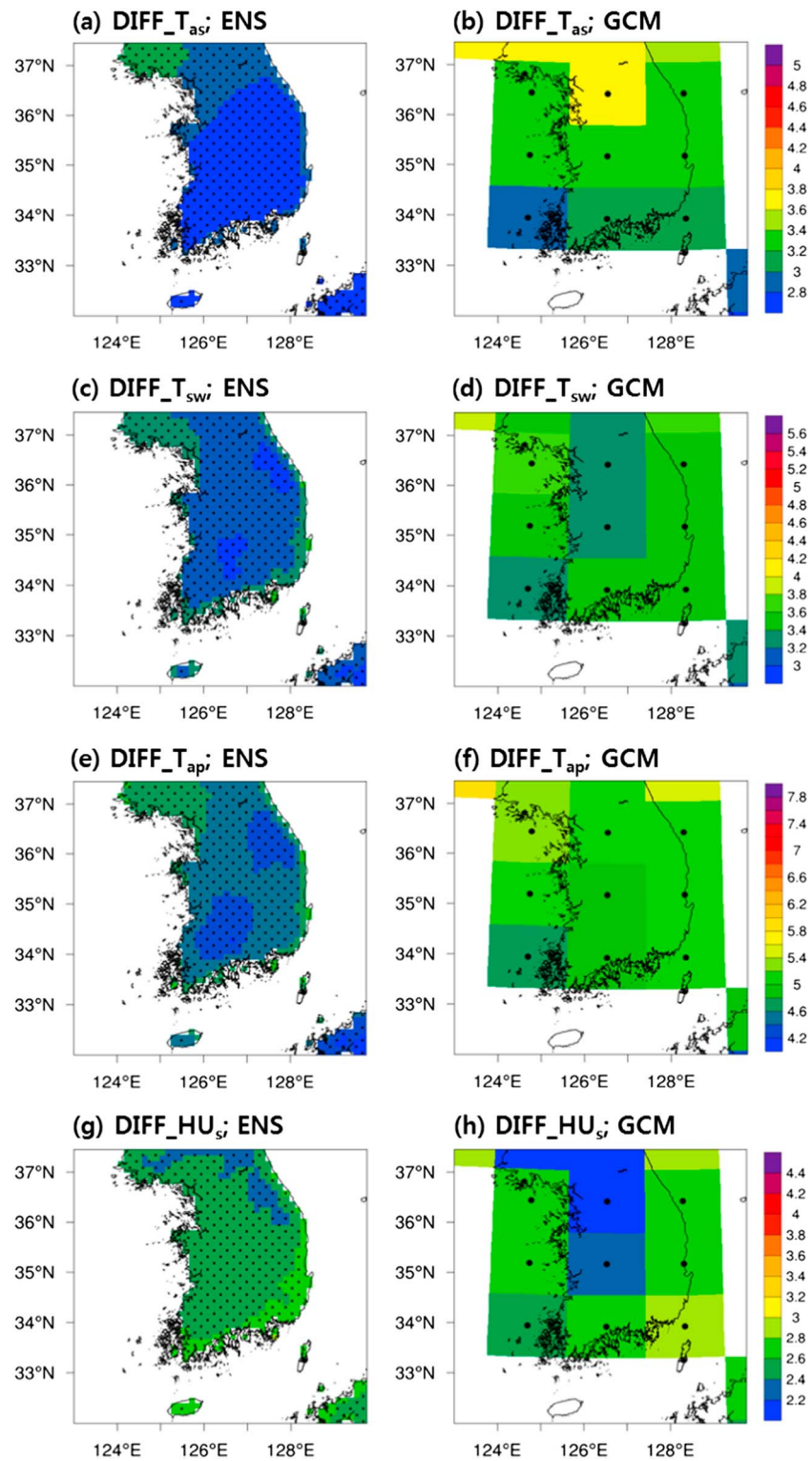
Figure 9. Spatial distribution of future changes (2071–2100 relative to 1981–2010 under RCP4.5) in summer daily mean (a, b: °C) T_{as}, (c, d: °C) T_{sw}, (e, f: °C) T_{ap}, and (g, h: g/kg) specific humidity derived from ENS (Figures 9a, 9c, 9e, and 9g) and GCM (Figures 9b, 9d, 9f, and 9h) projections. The superimposed dots denote the area where the changes are statistically significant at the 95% confidence level based on the Student's *t* test.
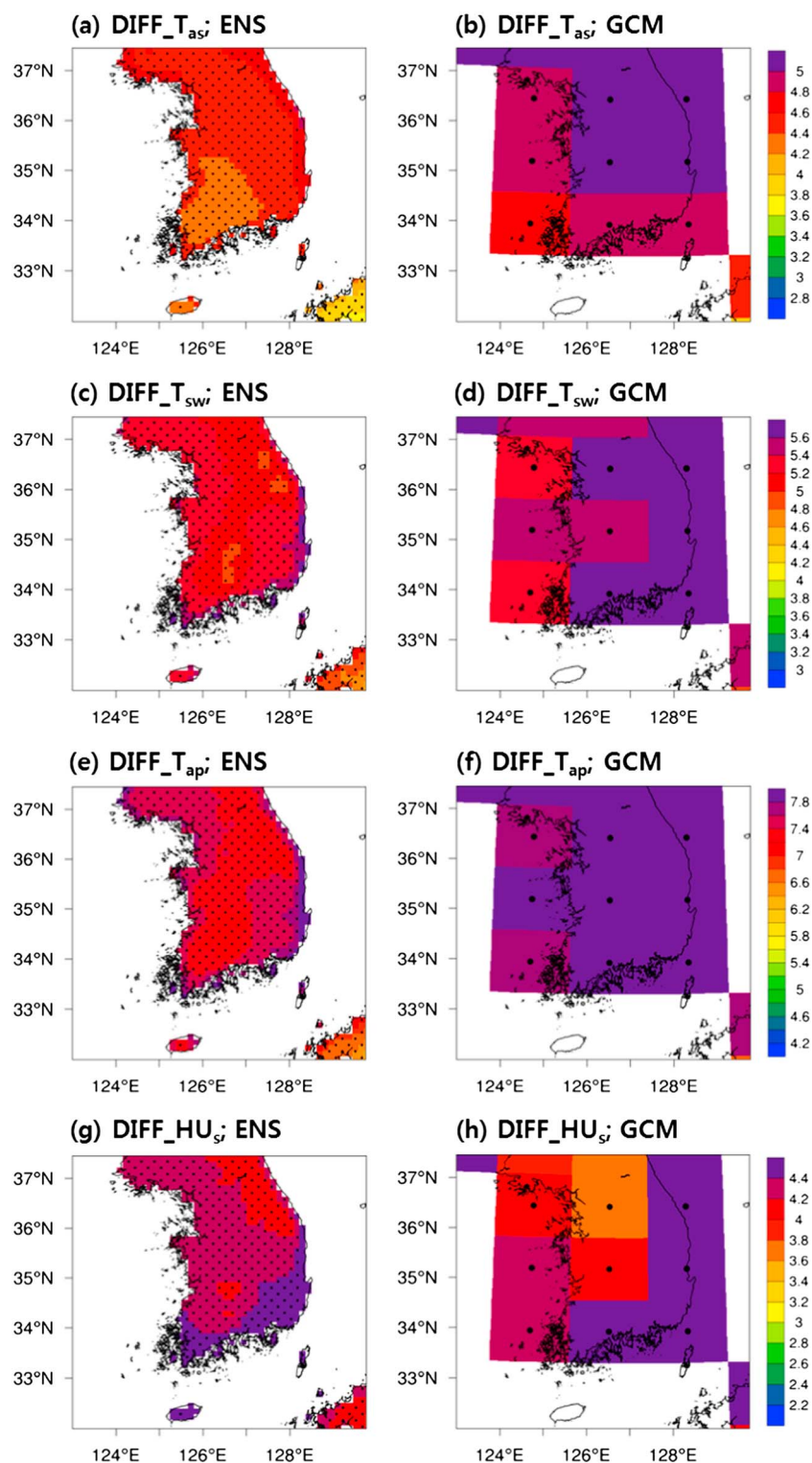
Figure 10. As in Figure 9 but for RCP8.5 scenario.

similarity and difference in their regional variations among T_{as}, T_{sw}, and T_{ap}. While T_{as} change shows an approximate southwest-northeast gradient pattern, T_{sw} and T_{ap} appear to be tied to topographic features. Compared to highly mountainous regions (e.g., the Taebaek Mountains and Sobaek Mountains, see Figure 1), the greater increases in T_{sw} and T_{ap} appear in low-elevation basins and coastal regions. This has
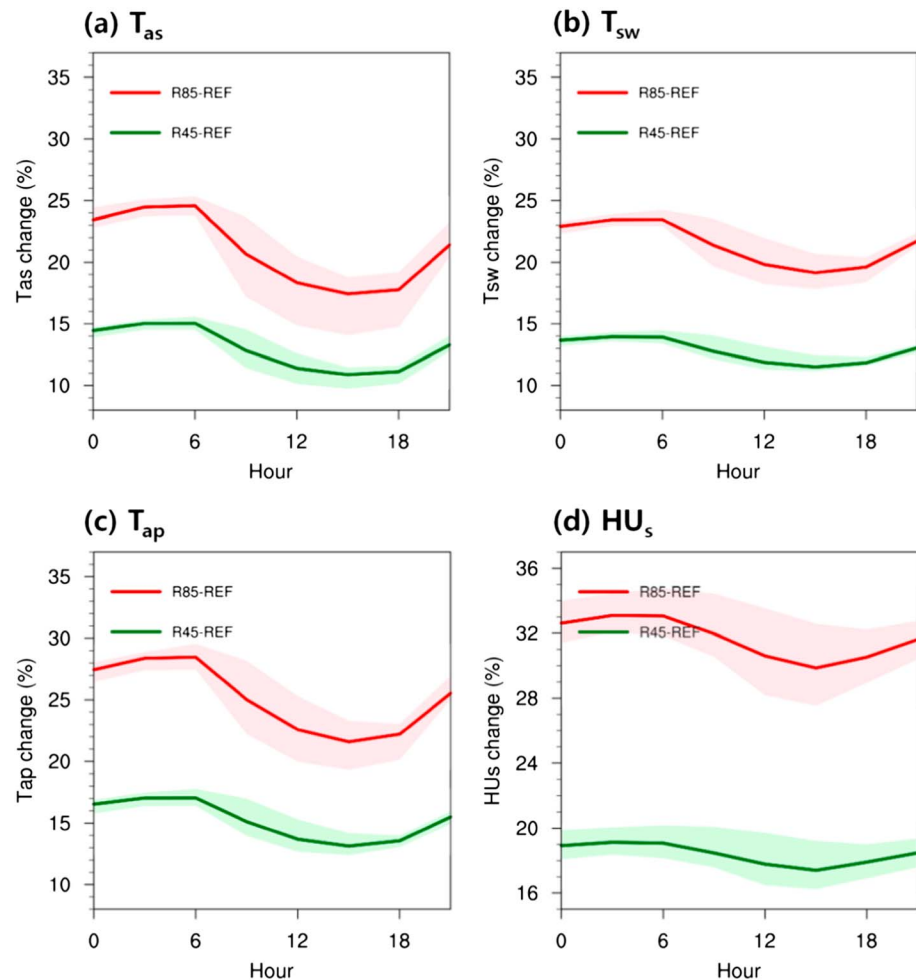
Figure 11. Future changes (2071–2100 relative to 1981–2010) in diurnal cycle of JJA mean (a) T_{as}, (b) T_{sw}, (c) T_{ap}, and (d) specific humidity averaged over 59 stations in South Korea. The green and red lines (shading) indicate changes derived from RCP4.5 and RCP8.5 ENS projections (intermodel spread), respectively.

important implications for the perspective of socioeconomic vulnerability and exposure at risk due to heat stress because the geographical locations of higher T_{sw} and T_{ap} coincide largely with regions of densely populated urban areas (Socioeconomic Data and Applications Center, http://sedac.ciesin.columbia.edu/). Along with rising temperature, significant increases in surface-specific humidity have been also identified in South Korea (Figures 9g and 10g). It is supported by the fundamental thermodynamics related to the Clausius-Clapeyron (C-C) relationship that atmospheric moisture-holding capacity increases approximately 7% for each 1 K increase in temperature. Significant deviations have been found in C-C scaling at the regional scale because this C-C relationship could be overwhelmed by other processes and factors (e.g., Ashfaq et al., 2016; Berg et al., 2009; Wang et al., 2017). However, Im et al. (2017) demonstrated that the temperature sensitivity of precipitation intensity roughly agrees with the C-C relationship over East Asia, including the Korean peninsula, using the same RCM projections analyzed in this study. The general similarity of spatial patterns between specific humidity and T_{sw} and T_{ap} suggests that atmospheric humidity is a key factor in shaping the geographical distribution of the increases in T_{sw} and T_{ap}. Therefore, increases in both temperature and humidity combine to favor higher heat stress indices such as T_{sw} and T_{ap} that include humidity effect, particularly in the low-elevation regions. This region-specific response of temperature and humidity due to global warming is an illustrative example that highlights the need for RCMs with a more refined representation of topography for climate change studies, particularly in regions like South Korea.

Figure 11 presents the changes in diurnal variations of T_{as}, T_{sw}, T_{ap}, and specific humidity in response to RCP4.5 and RCP8.5 emission scenarios. ENS and the intermodel spread are presented together. All
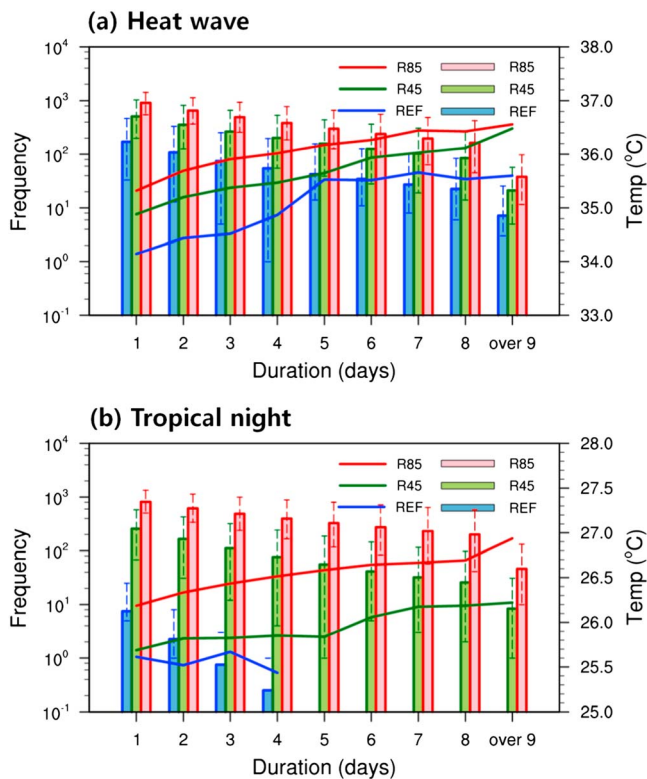
Figure 12. Frequency distribution of consecutive (a) heat waves and (b) tropical nights at various durations in Daegu station derived from reference simulation (1981–2010) and RCP4.5 and RCP8.5 projections (2071–2100). The colored lines indicate the daily maximum T_{as} (heat waves) and minimum T_{as} (tropical nights) averaged over each duration's frequency corresponding to the same color bar graph. Reference simulation results from the analysis of heat waves are the same as those presented in Figure 7.

variables show significant increases, the increments of which depend on the GHGs emission forcings, which is in line with the findings from Figures 9 and 10. In particular, specific humidity (more than 30%) is greatly increased under RCP8.5 scenario. The increasing rate of humidity with respect to temperature is approximately constrained by the C-C relationship, which shows an approximate 7% increase in the moisture holding capacity per degree Kelvin (K) increase. For example, while T_{as} increases by 2.8°C and 4.5°C under RCP4.5 and RCP8.5 scenarios (area-averaged values in Figures 9a and 10a), the daily mean-specific humidity increases by 18.4% and 31.7%, respectively, equating to 6.6% and 7% per K of warming, which are in good agreement with the C-C estimate (7%/K). As for the differentiated warming in diurnal cycle, the four RCMs show a fairly robust pattern in spite of intermodel deviation. Regardless of the degree of warming (RCP4.5 verus RCP8.5), all projections consistently show more increase in minimum peak and less increase in maximum peak. This implies that the increases in tropical nights defined by minimum T_{as} could be more dominant than the increases in heat waves defined by the maximum T_{as} under the warmer climate based on our RCM projections.

Figure 12 presents the frequency distribution of heat waves (i.e., maximum T_{as} exceeding 33°C) and consecutive tropical nights (i.e., minimum T_{as} exceeding 25°C) at various durations in Daegu station derived from reference simulation and RCP4.5 and RCP8.5 projections. As indicated by the validation of reference simulation, Daegu is one of the Korean regions most prone to extreme heat stress. Temperature increase is directly translated to the frequency and intensity of heat waves and consecutive tropical nights. As global warming strengthens, severe heat waves and tropical nights are projected to significantly increase. A notable change is the emergence of a long period of consecutive tropical nights even under RCP4.5 scenario. Compared to the changes in heat waves, tropical nights are projected to increase dramatically, which is consistent with the analysis of diurnal variation seen in Figure 11. Physiologically, the consecutive tropical nights will adversely affect human health by depriving comfortable sleep and inhibiting the recovery from the daytime heat stress. To investigate the severity of heat stress in days with tropical nights, we perform a composite analysis of heat stress indices. Simply, we divide daily mean T_{sw} and T_{ap} into two categories depending on whether or not the daily minimum temperature exceeds the threshold of tropical nights (25°C). The spatial distributions of daily mean T_{sw} and T_{ap} averaged over these two different categories are presented in Figures 13 and 14. Daily mean T_{sw} corresponding to tropical nights is much higher than that corresponding to nontropical nights. The behavior of T_{ap} is mostly similar with that of T_{sw}. Given that T_{sw} and T_{ap} combined with tropical nights show very consistent geographical patterns, the regions characterized by remarkably high T_{sw} and T_{ap} are far more likely to be adversely affected under future global warming. Assuming that humans suffer extreme heat stress all day long followed by tropical nights, the most severe impact will arise because heat stress is accumulated without the break or release period.

Figure 15 presents the spatial distribution of mean duration and intensity of heat waves defined as a spell of at least two consecutive days with maximum T_{ap} exceeding 33°C for the late 21st century (2071–2100) under RCP4.5 and RCP8.5 scenarios. This analysis further supports the conclusion already drawn from Figures 13 and 14: stronger emission forcing results in more extended duration and stronger intensity of heat waves. The pattern detected from the RCP4.5 projection is sufficiently strong to overwhelm the corresponding pattern from the reference simulation (not shown). The fact that the regions projected to undergo a greater increase of heat stress indices will also experience stronger, and more extended heat waves will impose much more significant risk and negative impact under global warming in South Korea.
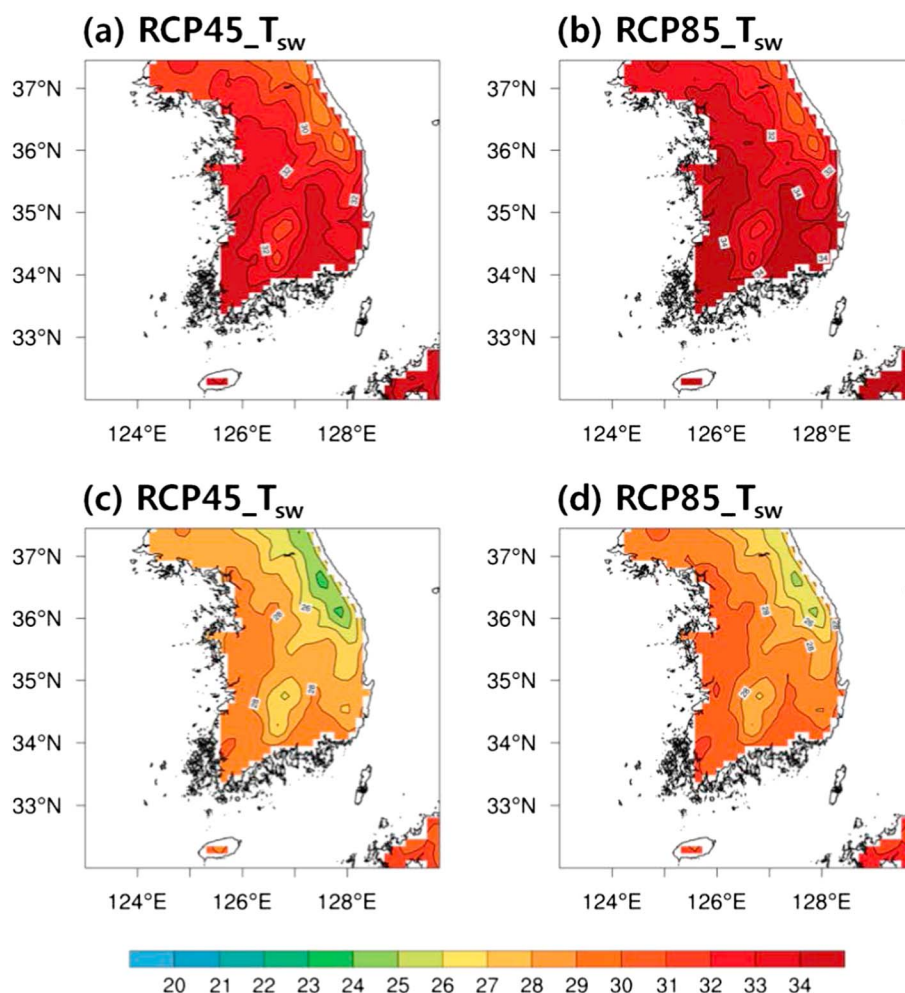
Figure 13. Composite map of T_{sw} (unit: °C) for (a, b) tropical nights and (c, d) nontropical nights derived from RCP4.5 and RCP8.5 ENS projections.

As an illustrative figure to emphasize the remarkable increase of heat stress under global warming, we generate the table of T_{sw} that mimics the National Weather Service Heat Index table provided by National Oceanic and Atmospheric Administration (http://www.nws.noaa.gov/om/heat/heat_index.shtml). Figure 16 describes T_{sw} with respect to temperature and humidity. The areas of T_{sw} above 26, 28, and 32°C are shaded with yellow, orange, and red colors, respectively, to indicate the level of risk as done by Willett and Sherwood (2012). We mark the maximum T_{sw} in the table after finding the corresponding temperature and humidity that are used to calculate the maximum T_{sw}. These are calculated by JJA averaged daily maximum for each year from the four individual RCMs (e.g., 30 × 4 = 120 values are plotted for each of HIS, RCP4.5, and RCP8.5). Therefore, these values represent the typical maximum condition, rather than very extreme cases that rarely happen. Tracking the movement of maximum T_{sw} corresponding to reference simulation and RCP4.5 and RCP8.5 projections clearly shows that global warming pushes T_{sw} into an area of extreme danger. To summarize, uncommonly high T_{sw} in the present-day climate will become characterized as normal under future global warming.

4. Summary and Discussion

Given that climate models show a robust pattern of temperature increase and a corresponding overall moistening in response to enhanced GHG forcing (IPCC, 2013; Sherwood et al., 2010), it is reasonable to expect that the future climate will increase the human thermal discomfort and heat-related mortality. However, in spite
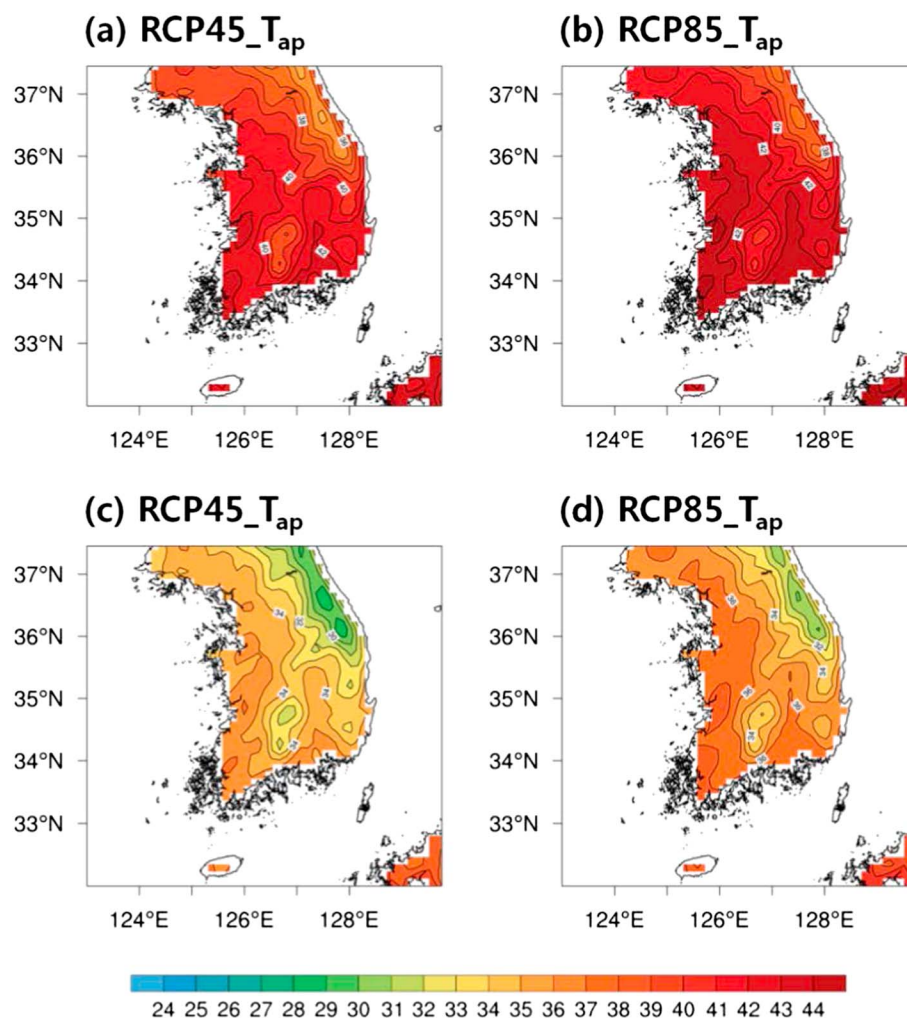
Figure 14. As in Figure 13 but for T_{ap} (unit: °C).

of a growing consensus on the future severity of extreme heat stress, the geographical patterns and magnitude of the projected changes remain poorly understood at the regional to local levels.

In this study, twelve 30 year multi-RCM projections (WRF, HadGEM3-RA, RegCM4, and MM5) driven by HadGEM2-AO global projections under multiscenarios of emissions (Reference, RCP 4.5 and RCP 8.5) are used to project and understand the changes in extreme heat stress in response to different levels of anthropogenic warming. High-resolution RCM results in terms of temporal (3 h) and spatial (12.5 km) scales make it possible to perform in-depth analysis such as diurnal variation and spatial details. The maximum and minimum T_{as}, T_{sw}, and T_{ap}, which are widely used as heat stress indices that include the effect of humidity, are comprehensively analyzed. For most of the analyses, both ENS and intermodel spread are presented, which is helpful in assessing the uncertainty introduced by different RCMs.

Based on extensive validation of the reference simulation against 59 in situ observational data, ENS is capable of capturing major characteristics in accordance with T_{as}, T_{sw}, and T_{ap}, in spite of some systematic cold bias. In particular, ENS shows an encouraging performance in simulating the extreme behavior of heat waves and heat stress indices in Daegu, a basin area that is one of the hottest cities in Korea. Moving to the future projection, significant increases of heat stress are projected in both RCP4.5 and RCP8.5 projections. The implied 2.4°C increase of mean T_{as} identified from the RCP4.5 projection is sufficiently strong to induce severe consequences in terms of human thermal comfort and heat-related mortality. This concern is supported by the notable increase of extreme heat stress indices, much stronger and more extended heat waves, and the emergence of a long period of consecutive tropical nights.
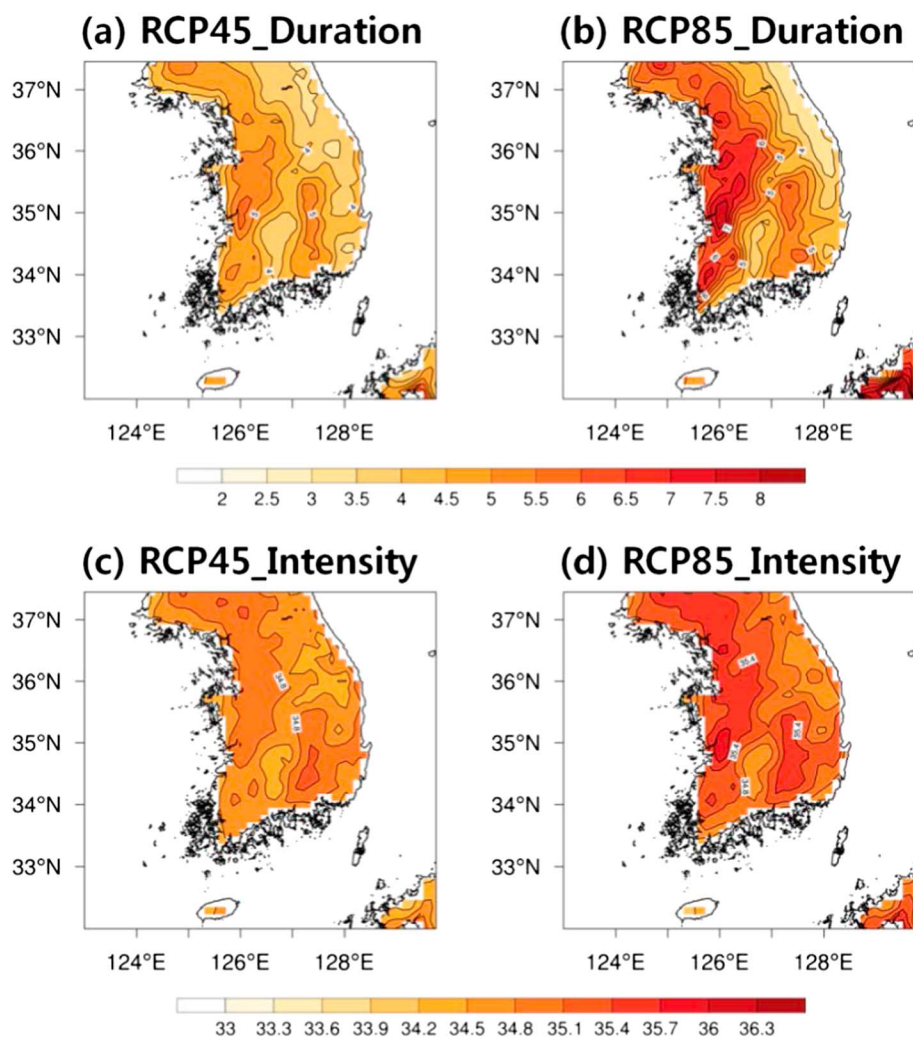
Figure 15. Spatial distribution of the (a, b) mean duration (unit: days) of heat waves and (c, d) T_{as} (unit: °C) averaged over heat waves derived from RCP4.5 (Figures 15a and 15c) and RCP8.5 (Figures 15b and 15d) ENS projections.

The present study supports the value in the dynamically downscaled RCM projections. Since the vulnerability to heat stress is regionally and topographically specific, it is difficult for GCMs with relatively coarse resolution to account for the unique geographical properties that potentially modulate the regional variation and intensity of heat stress in South Korea. In this regard, the ENS projection based on high-resolution multi-RCM has important implications for understanding and projecting the details of extreme heat stress, which in turn provides significant input to develop an adaptation strategy for related public health issues, outdoor workforce, and other infrastructure (e.g., electricity supply plans). As severe heat waves may become significant natural disasters with high mortality (Kysely & Kim, 2009), our study contributes to promoting further efforts and preparation for timely warning systems to cope with the region-specific impacts of global warming (Lu & Chen, 2016).

The four RCMs used in this study do not include the parameterization to represent the urban canopy process, suggesting that the projected increase of heat stress may be underestimated due to the urban heat island effect in big cities. Another possible caveat is that since T_{sw} and T_{ap} are empirical values based on different assumptions rather than fundamental thermodynamic metrics, they do not provide a universally applicable standard (Zhao et al., 2015). Therefore, the thresholds applied for this study (32°C for maximum T_{sw} and 40.6°C for maximum T_{ap}) are reference values for illustrative purposes. It is also difficult to use heat stress indices to ascertain the possible independent role of humidity and temperature (Davis et al., 2016).
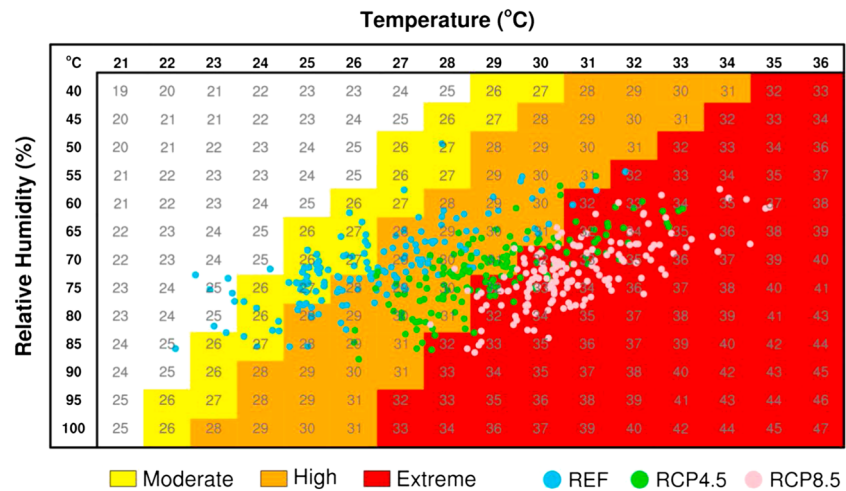
Figure 16. Table of simplified wet bulb globe temperature (T_{sw}, unit: °C) categorized by three risk levels. Summer mean daily maximum T_{sw} values in Daegu station (blue open circle in Figure 1) are displayed.

Nevertheless, it is generally accepted that these biometeorological indices, which include the humidity effect, are better indicators than mere maximum and minimum temperatures of the potential health impact and mortality associated with global warming (Anderson et al., 2013; Davis et al., 2016).

References

Ahn, J. B., Hong, J. Y., & Shim, K. M. (2016). Agro-climate changes over Northeast Asia in RCP scenarios simulated by WRF. *International Journal of Climatology*, *36*(3), 1278–1290. https://doi.org/10.1002/joc.4423

Ahn, J. B., Jo, S., Suh, M. S., Cha, D. H., Lee, D. K., Hong, S. Y., … Shim, K. M. (2016). Changes of precipitation extremes over South Korea projected by the 5 RCMs under RCP scenarios. *Asia-Pacific Journal of Atmospheric Sciences*, *52*(2), 223–236. https://doi.org/10.1007/s13143-016-0021-0

Anderson, G. B., Bell, M. L., & Peng, R. D. (2013). Methods to calculate the heat index as an exposure metric in environmental health research. *Environmental Health Perspectives*, *121*(10), 1111–1119. https://doi.org/10.1289/ehp.1206273

Ashfaq, M., Rastogi, D., Mei, R., Kao, S.-C., Gangrade, S., Naz, B. S., & Touma, D. (2016). High-resolution ensemble projections of near-term regional climate over the continental United States. *Journal of Geophysical Research: Atmospheres*, *121*, 9943–9963. https://doi.org/10.1002/2016JD025285

Baek, H. J., Lee, J., Lee, H. S., Hyun, Y. K., Cho, C. H., Kwon, W. T., … Byun, Y. H. (2013). Climate change in the 21st century simulated by HadGEM2-AO under representative concentration pathways. *Asia-Pacific Journal of Atmospheric Sciences*, *49*(5), 603–618. https://doi.org/10.1007/s13143-013-0053-7

Berg, P., Haerter, J. O., Thejll, P., Piani, C., Hagemann, S., & Christensen, J. H. (2009). Seasonal characteristics of the relationship between daily precipitation intensity and surface temperature. *Journal of Geophysical Research*, *114*, D18102. https://doi.org/10.1029/2009JD012008

Boo, K. O., Kwon, W. T., & Baek, H. J. (2006). Change of extreme events of temperature and precipitation over Korea using regional projection of future climate change. *Geophysical Research Letters*, *33*, L01701. https://doi.org/10.1029/2005GL023378

Buzan, J. R., Oleson, K., & Huber, M. (2015). Implementation and comparison of a suite of heat stress metrics within the community land model version 4.5. *Geoscientific Model Development*, *8*(2), 151–170. https://doi.org/10.5194/gmd-8-151-2015

Cha, D. H., & Lee, D. K. (2009). Reduction of systematic errors in regional climate simulations of the summer monsoon over East Asia and the western North Pacific by applying the spectral nudging technique. *Journal of Geophysical Research*, *114*, D14108. https://doi.org/10.1029/2008JD011176

Climate Council (2016). Global heat record broken again. Retrieved from http://www.climatecouncil.org.au/uploads/7ce0d94105bf486d5b598d1c928b51ee.pdf

Davies, T., Cullen, M. J. P., Malcolm, A. J., Mawson, M. H., Stainforth, A., White, A. A., & Wood, N. (2005). A new dynamical core for the Met Office's global and regional modelling of the atmosphere. *Quarterly Journal of the Royal Meteorological Society*, *131*(608), 1759–1782. https://doi.org/10.1256/qj.04.101

Davis, R. E., McGregor, G. R., & Enfield, K. B. (2016). Humidity: A review and primer on atmospheric moisture and human health. *Environmental Research*, *144*(Pt A), 106–116. https://doi.org/10.1016/j.envres.2015.10.014

Dunne, J. P., Stouffer, R. J., & John, J. G. (2013). Reductions in labour capacity from heat stress under climate warming. *Nature Climate Change*, *3*, 563–566. https://doi.org/10.1038/nclimate1827

Fischer, E. M., & Knutti, R. (2013). Robust projections of combined humidity and temperature extremes. *Nature Climate Change*, *3*(2), 126–130. https://doi.org/10.1038/nclimate1682

Fischer, E. M., Oleson, K. W., & Lawrence, D. M. (2012). Contrasting urban and rural heat stress responses to climate change. *Geophysical Research Letters*, *39*, L03705. https://doi.org/10.1029/2011GL050576

Fischer, E. M., & Schar, C. (2010). Consistent geographical patterns of changes in high-impact European heatwaves. *Nature Geoscience*, *3*(6), 398–403. https://doi.org/10.1038/ngeo866

Giorgi, F., Coppola, E., Solmon, F., Mariotti, L., Sylla, M. B., Bi, X., … Brankovic, C. (2012). RegCM4: Model description and preliminary test over multiple CORDEX domains. *Climate Research*, *52*, 7–29. https://doi.org/10.3354/cr01018

Hawkins, E., & Sutton, R. (2009). The potential to narrow uncertainty in regional climate predictions. *Bulletin of the American Meteorological Society*, *90*(8), 1095–1107. https://doi.org/10.1175/2009BAMS2607.1

Hong, J. Y., & Ahn, J. B. (2015). Changes of early summer precipitation in the Korean Peninsula and nearby regions based on RCP simulations. *Journal of Climate*, *28*(9), 3557–3578. https://doi.org/10.1175/JCLI-D-14-00504.1

Im, E. S., Ahn, J. B., & Jo, S. R. (2015). Regional climate projection over South Korea simulated by the HadGEM2-AO and WRF model chain under the RCP emission scenarios. *Climate Research*, *69*, 249–266.

Im, E. S., Jung, I. W., & Bae, D. H. (2011). The temporal and spatial structure of recent and future trends in extreme indices over Korea from a regional climate projection. *International Journal of Climatology*, *31*(1), 72–86. https://doi.org/10.1002/joc.2063

Im, E. S., Choi, Y. W., & Ahn, J. B. (2017). Robust intensification of hydroclimatic intensity over East Asia from multi-model ensemble regional projections. *Theoretical and Applied Climatology*, *129*(3-4), 1241–1254. https://doi.org/10.1007/s00704-016-1846-2

IPCC (2013). Climate change 2013: The physical science basis. In T. F. Stocker, et al. (Eds.), *The Fifth Assessment Report of the Intergovernmental Panel on Climate Change* (pp. 161–162). Cambridge, UK, and New York: Cambridge University Press.

Kim, H., Ha, J. S., & Park, J. (2006). High temperature, heat index, and mortality in 6 major cities in South Korea. *Archives of Environmental & Occupational Health*, *61*(6), 265–270. https://doi.org/10.3200/AEOH.61.6.265-270

Koo, G. S., Boo, K. O., & Kwon, W. T. (2009). Projection of temperature over Korea using an MM5 regional climate simulation. *Climate Research*, *40*, 241–248. https://doi.org/10.3354/cr00825

Korea Meteorological Administration (KMA) (2017). 2016: Abnormal Climate Report, KMA Publ., pp. 192.

Kysely, J., & Kim, J. (2009). Mortality during heat waves in South Korea, 1991 to 2005: How exceptional was the 1994 heat wave. *Climate Research*, *38*, 105–116. https://doi.org/10.3354/cr00775

Lee, J. W., Hong, S. Y., Chang, E. C., Suh, M. S., & Kang, H. S. (2014). Assessment of future climate change over East Asia due to the RCP scenarios downscaled by GRIMs-RMP. *Climate Dynamics*, *42*(3-4), 733–747. https://doi.org/10.1007/s00382-013-1841-6

Lemke, B., & Kjellstrom, T. (2012). Calculating workplace WBGT from meteorological data: A tool for climate change assessment. *Industrial Health*, *50*(4), 267–278. https://doi.org/10.2486/indhealth.MS1352

Lu, R., & Chen, R. (2016). A review of recent studies on extreme heat in China. *Atmospheric and Oceanic Sciences Letters*, *9*(2), 114–121. https://doi.org/10.1080/16742834.2016.1133071

Meehl, G. A., & Tebaldi, C. (2004). More intense, more frequent, and longer lasting heat waves in the 21st century. *Science*, *305*(5686), 994–997. https://doi.org/10.1126/science.1098704

Min, S. K., Kim, Y. H., Kim, M. K., & Park, C. (2014). Assessing human contribution to the summer 2013 Korean heat wave. *Bulletin of the American Meteorological Society*, *95*, S48–S51.

Moss, R. H., Edmonds, J. A., Hibbard, K. A., Manning, M. R., Rose, S. K., van Vuuren, D. P., … Wilbanks, T. J. (2010). The next generation of scenarios for climate change research and assessment. *Nature*, *463*(7282), 747–756. https://doi.org/10.1038/nature08823

Seo, Y. A., Lee, Y., Park, J. S., Kim, M. K., Cho, C., & Baek, H. J. (2015). Assessing changes in observed and future projected precipitation extremes in South Korea. *International Journal of Climatology*, *35*(6), 1069–1078. https://doi.org/10.1002/joc.4039

Sherwood, S. C., & Huber, M. (2010). An adaptability limit to climate change due to heat stress. *Proceedings of the National Academy of Sciences*, *107*(21), 9552–9555. https://doi.org/10.1073/pnas.0913352107

Sherwood, S. C., Roca, R., & Weckwerth, T. M. (2010). Tropospheric water vapor, convection, and climate. *Reviews of Geophysics*, *48*, RG2001. https://doi.org/10.1029/2009RG000301

Skamarock, W., Klemp, J., Dudhia, J., Gill, D., Barker, D., Wang, W., & Powers, J. (2008). A description of the advanced research WRF version 3 (NCAR Tech. Note NCAR/TN-475+STR). Boulder, CO: NCAR.

Son, J.-Y., Lee, J.-T., Anderson, G. B., & Bell, M. L. (2012). The impact of heat waves on mortality in seven major cities in Korea. *Environmental Health Perspectives*, *120*(4), 566–571. https://doi.org/10.1289/ehp.1103759

Steadman, R. G. (1984). A universal scale of apparent temperature. *Journal of Climate and Applied Meteorology*, *23*(12), 1674–1687. https://doi.org/10.1175/1520-0450(1984)023%3C1674:AUSOAT%3E2.0.CO;2

Steinweg, C., & Gutowski, W. J. (2015). Projected changes in greater St. Louis summer heat stress in NARCCAP simulations. *Weather, Climate, and Society*, *7*(2), 159–168. https://doi.org/10.1175/WCAS-D-14-00041.1

Suh, M. S., & Kim, C. (2015). Change-point analysis of tropical night occurrences for five major cities in Republic of Korea. *Advances in Meteorology*, *2015*, 801981

Suh, M. S., Oh, S. G., Lee, Y. S., Ahn, J. B., Cha, D. H., Lee, D. K., … Kang, H. S. (2016). Projections of high resolution climate changes for South Korea using multiple-regional climate models based on four RCP scenarios. Part 1: Surface air temperature. *Asia-Pacific Journal of Atmospheric Sciences*, *52*(2), 151–169. https://doi.org/10.1007/s13143-016-0017-9

Wang, G., Wang, D., Trenberth, K. E., Erfanian, A., Yu, M., Bosilovich, M. G., & Parr, D. T. (2017). The peak structure and future changes of the relationships between extreme precipitation and temperature. *Nature Climate Change*, *7*(4), 268–274. https://doi.org/10.1038/nclimate3239

Willett, K. M., & Sherwood, S. (2012). Exceedance of heat index thresholds for 15 regions under a warming climate using the wet-bulb globe temperature. *International Journal of Climatology*, *32*, 430–440.

Willett, K. W., Jones, P. D., Gillett, N. P., & Thorne, P. W. (2008). Recent changes in surface humidity: Development of the HadCRUH dataset. *Journal of Climate*, *21*(20), 5364–5383. https://doi.org/10.1175/2008JCLI2274.1

Wu, J., Gao, X., Giorgi, F., & Chen, D. (2017). Changes of effective temperature and cold/hot days in late decades over China based on a high resolution gridded observation dataset. *International Journal of Climatology*, *37*(S1), 788–800. https://doi.org/10.1002/joc.5038

Yasutomi, N., Hamada, A., & Yatagai, A. (2011). Development of a long-term daily gridded temperature dataset and its application to rain/snow discrimination of daily precipitation. *Global Environmental Research*, *15*, 165–172.

Zhao, Y., Ducharne, A., Sultan, B., Braconnot, P., & Vautard, R. (2015). Estimating heat stress from climate-based indicators: Present-day biases and future spreads in the CMIP5 global climate model ensemble. *Environmental Research Letters*, *10*, 084013(8). https://doi.org/10.1088/1748-9326/10/8/084013